Network hydration, ordering and composition interplay of chemical vapor deposited amorphous silica films from tetraethyl orthosilicate

Babacar Diallo, Konstantina Christina Topka, Maxime Puyo, Charlotte Lebesgue, Cecile Genevois, Raphaël Laloo, Diane Samélor, Helene Lecoq, Mathieu Allix, Hugues Vergnes, et al.

Available online at www.sciencedirect.com

jmr&t Journal of Materials Research and Technology

journal homepage: www.elsevier.com/locate/jmrt

Original Article

Network hydration, ordering and composition interplay of chemical vapor deposited amorphous silica films from tetraethyl orthosilicate

Babacar Diallo [a,1], *Konstantina C. Topka* [b,c,1], *Maxime Puyo* [b], *Charlotte Lebesgue* [b], *Cécile Genevois* [a], *Raphael Laloo* [b], *Diane Samelor* [b], *Hélène Lecoq* [a], *Mathieu Allix* [a], *Hugues Vergnes* [c], *François Senocq* [b], *Pierre Florian* [a], *Vincent Sarou-Kanian* [a], *Thierry Sauvage* [a], *Marie-Joelle Menu* [b], *Brigitte Caussat* [c], *Viviane Turq* [b], *Constantin Vahlas* [b], *Nadia Pellerin* [a,*]

[a] *CNRS, Conditions Extrêmes et Matériaux: Haute Température et Irradiation (CEMHTI) UPR 3079, Université d'Orléans, Orléans, France*

[b] *Centre Interuniversitaire de Recherche et d'Ingénierie des Matériaux (CIRIMAT), Université de Toulouse, CNRS, Toulouse, France*

[c] *Laboratoire de Génie Chimique (LGC), Université de Toulouse, CNRS, Toulouse, France*

ARTICLE INFO

Article history:
Received 10 December 2020
Accepted 25 April 2021
Available online 30 April 2021

Keywords:
CVD
SiO_2
Hydrated species
Network ordering
Etching rate
Mechanical properties

ABSTRACT

The chemical or mechanical performance of amorphous SiO_2 films depend on intrinsic physicochemical properties, which are intimately linked to atomic and molecular arrangements in the Si–O–Si network. In this context, the present work focuses on a comprehensive description of SiO_2 films deposited from a well-established chemical vapor deposition process involving tetraethyl-orthosilicate, oxygen and ozone, and operating at atmospheric pressure in the range 400–550 °C. The connectivity of the silica network is improved with increasing the deposition temperature (T_d) and this is attributed to the decreased content of hydrated species through dehydration-condensation mechanisms. In the same way, the critical load of delamination increases with increasing T_d thanks to the silicon substrate oxidation. The utilization of a O_2/O_3 oxidizing atmosphere involving the oxidation of intermediates species by O_2, O_3 and $O^{\cdot}$, allows increasing the deposition rate at moderate temperatures, while minimizing carbon, H_2O and silanol contents to extremely low values (4.5 at.% of H). The SiO_x stoichiometry and T_d interplay reveals two distinct behaviors before and above 450 °C. The best corrosion resistance of these films to standard P-etching test is obtained for the minimum silanol content and the best network molecular ordering, with an etching rate of 4.0 ± 0.1 Å/s at pH = 1.5. The elastic modulus and hardness of the films remain stable in the investigated range of deposition temperature, at 64.2 ± 1.7 and 7.4 ± 0.3 GPa respectively, thanks to the low content in silanol groups.

* Corresponding author.
E-mail address: nadia.pellerin@univ-orleans.fr (N. Pellerin).
[1] Co-first authors: Babacar Diallo and Konstantina C. Topka.

https://doi.org/10.1016/j.jmrt.2021.04.067

1. Introduction

Since the seventies, SiO_2-based films have received much attention due to their well-established properties for electrical, optical, magnetic or barrier applications in most Key Enabling Technologies [1–4]. In particular, amorphous SiO_2 films are largely used as dielectric materials in electronic and optoelectronic devices [4–6], or as gas diffusion barrier on various plastic packaging materials [7]. For these and other applications, the chemical durability of the SiO_2 films is a major parameter, which is intimately linked to atomic and molecular arrangements in the Si–O–Si network, associated with the short (over 1.5–2.5 Å) and medium- (over 2.5–4.5 Å) range orders, respectively, investigated by nuclear magnetic resonance or infrared spectroscopy, for instance [8–10]. Indeed, investigations of the medium-range order in glass networks revealed that chemical durability depends on the film molecular structure and composition through the distribution of hydrolysis sites and the subsequent access of water to these sites. At least four mechanisms control the glass durability, namely (i) ion exchange in presence of modifier cations, e.g. alkali or alkaline earth ions; (ii) hydration through the diffusion of hydrated species; (iii) accelerated matrix dissolution by hydrolysis; and (iv) formation of a passivating surface layer [11–14]. Then, Osseo-Asare [15] has underlined the contribution of the surface chemistry and suggested pH dependent protonation and deprotonation of the surface silanol groups to give positively ($Si–OH_2^+$) and negatively (SiO^-) charged sites respectively. By way of comparison, the dissolution rates of quartz and amorphous silica in pure water are 4.2×10^{-14} and 9.0×10^{-13} mol/m^2 s, respectively, and their solubility stays very low for pH < 9 [16,17]. The difference in these dissolution rates can be explained by the network geometry dependence of the dissolution kinetics, which imply that some surface bonding geometries react more readily than others [18]. This dependency elevates the film density and the degree of ordering of the Si–O–Si network as the main parameters that affect the dissolution of the SiO_2 films. In the same way, considering the mechanical properties of glasses, elastic moduli and Young's modulus in particular, do not solely depend on the interatomic bonding energy but also depend on the coordination, on the polymerization degree (cross linking), on the atomic packing density, and on the molecular organization [10]. It thus appears that in-depth knowledge of the structure of SiO_2 films and its twofold comprehensive correlation with the targeted functional properties and the processing conditions are essential for developing further all advanced applications.

Optical [19], fouling and corrosion [20], barrier [21] or electrical [22] properties of SiO_2 films produced through a variety of processes are continuously studied in the literature to this day. However, few of them focus on the structural organization of the SiO_2 network, especially in terms of its hydration. In a recent study, Jung et al. [23] studied the dielectric properties of SiO_2 films by plasma enhanced chemical vapor deposition (PECVD) and plasma enhanced atomic layer deposition (PEALD) from bis(diethylamino)silane ($H_2Si[N(C_2H_5)_2]_2$, BDES) O_2, intended for flexible and thin-film-transistor (TFT) devices, based on their chemical composition and growth characteristics. The authors reported decreased leakage currents at higher substrate temperatures, correlating this to an improvement of SiO_2 film stoichiometry at elevated temperatures. Measured by X-ray photoelectron spectroscopy (XPS) however, their stoichiometry values do not account for hydrated species. More recently, Kim et al. [24] performed deposition of high quality SiO_2 films from 1,2-bis-(diisopropylamino)disilane (BDIPADS) and ozone, using thermal atomic layer deposition (ALD). The authors investigated the chemical and electrical characteristics of the SiO_2 films, observing slight degradation in the dielectric constants, leakage currents, and breakdown fields with decreasing deposition temperature. The authors attributed this to slight decrease in film density with parallel increased defect density of Si–H related bonds. Specifically, they noted the presence of the $(O–)_3Si–H$ bending mode at 880 cm^{-1} at low temperatures and its disappearance at higher growth temperatures, giving in turn rise to the Si–O–Si bend vibrational mode at 800 cm^{-1}. However, quantitative information on the level of network hydration are not reported.

Securing long-term performance of such devices and systems also relies on their mechanical properties (hardness, elastic modulus, scratch resistance), which are heavily influenced by the deposition process. As pointed out by Simurka et al. [25], the mechanical properties of SiO_2 films vary largely in the literature. In their own study, hardness and elastic modulus were noted to decline from 8.5 to 2.2 GPa and from 73.7 to 30.9 GPa, respectively, with increase of the process pressure. The authors attributed this decrease to the less dense structure of the films prepared at higher process pressure, with these films also exhibiting absorptions related to hydrogen-bonded hydroxyl groups and adsorbed water. Quantitative data on the amount of hydrogen incorporated in the SiO_2 films were not given however.

The present work aims to bridge this gap, by correlating process conditions and functional properties to the molecular organization, structure and network hydration of SiO_2 films, subscribing to the requirements for an in-depth understanding of the material in view of advanced applications. We have processed SiO_2 films by oxygen-ozone O_2/O_3 mixture assisted atmospheric pressure chemical vapor deposition (CVD) from tetraethyl orthosilicate ($Si(OC_2H_5)_4$,TEOS), a well-established robust and scalable route, operating at low to moderate temperatures (400–550 °C). Despite the popularity of this process, the film quality is questionable, depending in particular on the T_d, which modifies the gaseous intermediate species generated from the decomposition of TEOS, and their subsequent involvement in the formation of the film [26]. Indeed, the high thermal and chemical stability and fracture toughness of silica [27,28] does not prevent the occurrence of defects that can still be present, along with sub- or over-stoichiometry [29,30]. Especially, SiO_2 films deposited below 450 °C often contain carbon-related impurities and trapped charges leading to oxygen deficiency [31] and subsequently to degraded capacitance–voltage and current density–electric field behaviors, or to increased etching rate. The dependence between the oxidation and dehydration mechanisms on the one hand and the oxidant gas nature or the working temperature on the other hand, are not entirely understood. In particular, the role of O_2 and O_3 in the

production of oxygen radicals for the oxidation of TEOS and of secondary products is not clear, despite the development of apparent kinetic models able to predict the silica deposition rates and the local profiles of gas flow and temperature in the reactor, for instance [26,32]. Also, the nature and the quantity of hydrated species and their impact on the SiO_x stoichiometry are poorly investigated and are not well known. In this perspective, in the present work we probed the hydrated species in the films and correlated these with the SiO_x stoichiometry and T_d in the range between 400 and 550 °C.

We have analyzed the films by Fourier transform infrared (FTIR) spectroscopy to get insight in the short and medium range order structure and in the nature of hydrated species. We have combined this information with input from high-resolution transmission electron microscopy (HRTEM), ion beam analysis (IBA), time-of-flight secondary ion mass spectrometry (ToF-SIMS) and XPS. These investigations have allowed insight in the O/Si ratio and the concentration of hydrated species explored along the film depth profile, and on the connectivity of the Si–O–Si network. We have correlated these chemical and structural characteristics with the mechanical and surface properties of the films, namely their hardness, Young modulus and critical load of delamination probed by nanoindentation and nanoscratch, as well as their wettability and their etching rate in standard hydrofluoric acid (HF) solutions.

2. Materials and methods

CVD of amorphous SiO_2 films was performed in a horizontal, tubular, hot-wall reactor. The experimental setup for the deposition of SiO_2 films is schematically illustrated in Fig. 1 and has been developed previously [26]. The experiments were performed at four different T_d, namely 400, 450, 500 and 550 °C, defined as the temperature measured at the middle of the reactor, where an isothermal region exists. TEOS and O_2/O_3 flow rates were respectively 2 standard cubic centimeters per minute (sccm) and 1960 sccm (O_3 concentration of 60 mg/l) and a deposition time of 30 min was considered providing film thickness of approximatively 100 nm. Thicker films of about 300–400 nm have also been used for nanoindentation testing. The SiO_2 deposition rates were calculated from the weight difference before and after deposition, by measuring the deposited mass using a Sartorius Genius Series ME215P instrument with 0.015 mg precision.

280 μm thick monocrystalline silicon (100) wafers (Neyco S.A.), cut in rectangles of 32 × 24 mm^2, were used as substrates. They were supported vertically by two custom-made substrate holders placed in the isothermal region [26].

The films thickness was estimated by ellipsometry, with a Semilab SE-2000 instrument, operating between 250 and 1000 nm wavelength range, using a constant incidence angle of 70°. The measurements were performed by probing 3 points vertically along the surface's center of each sample. The spectroscopic ellipsometry data were simulated and fitted in the 250–1000 nm wavelength range using the Semilab SEA software. The calculated results were collected for a linear regression R^2 fit of over 0.99. Water content was evaluated using the Bruggeman effective medium approximation (BEMA) model, applying a three components medium, including SiO_2, void and H_2O. The Sellmeier model was used as a reference to confirm the measured local thickness. The above models were validated by measuring the cross-section of one representative sample by a FEI Quanta450 scanning electron microscope (SEM).

The surface's roughness of the films was measured using a Bruker Dimension ICON, Nanoscope V atomic force microscopy (AFM) operating in tapping mode. The tip used was a TESPA V2 from Bruker, made of n-doped silicon, with a radius <10 nm. A scan size of 1 μm^2 was implemented for all measurements.

The chemical composition of the films (carbon, hydrogen content and O/Si atomic ratio) was determined by using IBA. Silicon, oxygen and hydrogen contents were determined by Rutherford backscattering spectroscopy (RBS), nuclear reaction analysis (NRA) and elastic recoil detection analysis (ERDA), respectively. RBS was performed at a 166° detection angle with 2 MeV α particles. Oxygen concentration was measured through the $^{16}O(d,\alpha_0)^{14}N$ nuclear reaction using incident deuterons of 0.9 MeV and emitted alpha particles detected in the previous configuration at a 166° angle. ERDA measurements were performed with 2.8 MeV alpha beam. The sample was positioned at 15° grazing incidence angle and the recoiled hydrogen atoms were collected at a scattering angle of 30°. The composition of the films was obtained by simulation of the RBS, NRA and ERDA spectra using the SIMNRA

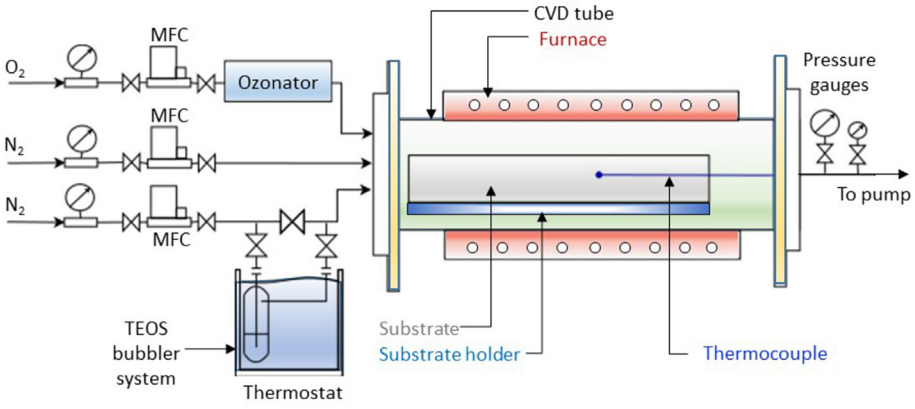

Fig. 1 – Schematic representation of the horizontal CVD reactor.

software [33]. A polycrystalline silicon wafer with a top layer of 213 nm SiO_2 film and a-Si(H^+) hydrogen standard at 2.19×10^{17} H/cm^2, a carbon and a SiC polycrystalline films were used for the energy calibration of the detector [34].

Complementary chemical analysis was performed by XPS depth profiles using a NOVA-KRATOS instrument. The profiles were recorded under monochromatic Al-Kα radiation of 225 W, on a 110×110 μm^2 area (μspot mode) for a depth lower than 10 nm. A 1.5×1.5 mm^2 surface was sputtered with Ar_{500+} argon plasma cluster with an energy of 20 keV. A sputtering rate of 0.10 nm/s was deduced from thickness measurements determined by ellipsometry. The atomic concentrations profiles of silicon, oxygen and carbon were analyzed in low-resolution mode from individual spectra considering Si 2p, C 1s and O 1s peaks. In addition, high resolution spectra were obtained with monochromatic Al-Kα radiation of 150 W from an analyzed area of 300×700 μm^2. SiO_2 films were then characterized by survey scans and quantitative analysis for Si 2p, O 1s and C 1s peaks areas corrected by their appropriate sensitivity factors ($S_{Si} = 0.328$, $S_O = 0.780$ and $S_C = 0.278$).

ToF-SIMS analysis was performed on an IONTOF TOF 5 instrument. An Ar^+ ion beam of 20 keV and 12 nA was used for surface abrasion (500×500 μm^2). The analysis was then provided by a Bi_3^+ ion sputtering beam (25 keV, ~0.2 pA, 100×100 μm^2) followed by ToF investigation of secondary ions extracted from the samples. The surface was neutralized during analysis by a low-energy electron flux (<20 eV). The depth of the final crater was measured using a 3D profilometer, allowing elemental profile depth calibration. The following species profiles were selected for analysis: O^-, OH^-, Si^-, SiO_2^-, SiO_3^-, $SiHO_2^-$, $SiHO_3^-$ and $Si_2HO_5^-$. These profiles were then normalized to that of Si^- to avoid matrix effects, taking into account the low mobility and the abundance of silicon [35]. The following formula was used for this purpose:

$$Jn_i^a = J_i^a / J_i^{Si^-} \quad (1)$$

where Jn_i^a is the normalized intensity of an element a, and J_i^a and $J_i^{Si^-}$ are the as-measured intensities at a point i of the profile for the elements a and Si^-.

The nanostructure of the films was investigated by TEM. Chemical information was obtained by scanning transmission electron microscopy-high angle annular dark field (STEM-HAADF) imaging, STEM-EDS profiles, and electron energy loss spectroscopy (EELS). The acquisition was carried out with a JEOL-ARM200 Cold FEG microscope operating at 80 keV, equipped with double spherical aberration correctors and fitted with a JEOL SDD CENTURIO EDS system and a Gatan GIF Quantum. The samples were prepared by focused ion beam (FIB) technique using a Helios machine. The selected areas were covered by protective layers of carbon (50 nm) and platinum (3 μm). The samples were trimmed using Ga^+ ions until they became transparent to the electrons with a uniform thickness (≈50 nm). TEM analyses were performed immediately after the FIB preparation to avoid contamination.

FTIR spectrometry study was performed in transmission mode with a Frontier FTIR MIR/NIR spectrometer, using a custom-made substrate holder that enabled the analysis at different angles. The spectra were taken with a 60° angle (Brewster angle) between the sample and the incident beam, to clearly observe TO-LO splitting. The spectral range 400–4000 cm^{-1} was probed with a 4 cm^{-1} spectral resolution. Sixteen spectra accumulations were taken for each sample, after removal of the background signal. Upon acquisition, the obtained spectral data were further processed by removing substrate signature and correcting the baseline. Finally, absorbance values were normalized by each film thickness, since SiO_2 peak intensities are affected by the thickness of the film in transmission mode [9,36].

Nanoindentation tests were carried out using an Ultra-NanoIndenter apparatus from CSM Instruments (Anton Paar) with a Berkovich diamond indenter. For nanoindentation, the load was gradually increased until a maximum value of 0.5 mN, at which the load was maintained for 30 s, and then decreased down to zero. The loading and unloading rate was 1 mN/min. The system has typical load and displacement resolutions of 0.25 μN and 0.1 nm respectively. Elastic modulus and hardness were calculated from the load vs. depth curves with the method proposed by Oliver and Pharr [37]. For these tests, films with a higher thickness of about 500 nm were used in order to limit the substrate contribution. The standard deviation for elastic Young's modulus and hardness measurements are 1.7 and 0.3 GPa respectively.

Nanoscratch tests were conducted using a Nanoscratch Tester from CSM Instrument (Anton Paar) equipped with a spherical diamond indenter (radius 2 μm). Scratches were made under linearly increasing load from 0.3 to 100 mN with an increasing loading rate of 20 mN/min with a displacement speed of 1 mm/min. Three measurements were carried out at different locations on each sample to assess the repeatability. Optical microscope (Nanoscratch CSM) and SEM (Vega 3 TESCAN) were used to analyze the tracks and determine the critical normal loads corresponding to coating adhesive failures.

Wettability was evaluated by measuring pure water contact angle with a GBX apparatus. Water droplets of 0.35 ± 0.01 μl were placed slowly and carefully onto the surface at ambient atmosphere and temperature, and the equilibrium static contact angle was measured using a CCD camera at five different locations on each sample, with 0.8–1.1° uncertainty.

The etching rate of the films was evaluated using the P-etch test developed by Pliskin [38]. The test is performed at pH = 1.5 by partly immerging the sample in a solution of 3 parts of hydrofluoric acid (49 wt.%), 2 parts of nitric acid (70 wt.%), and 60 parts of distilled water. Immersion was maintained for 30 s, under continuous stirring of the solution at 25 °C. The P-etching rate for each sample, expressed in Å/s, was determined through reflection spectroscopic ellipsometry, by measuring the thickness before and after immersion.

3. Results

3.1. Microstructure and medium range order

A film deposited at $T_d = 500$ °C was analyzed by TEM, XPS and ToF-SIMS and the results are resumed in Fig. 2. Its thickness is 119 ± 5 nm in the observed area and no specific defect, texture or nanoporosity is noted (Fig. 2a), as classically observed for such SiO_2 CVD films. On Fig. 2b, the EELS analysis reveals a uniform distribution of the oxygen content throughout the

layer. The ADF image confirms the chemical homogeneity and shows a thin bright line that could indicate internal strengths in the silicon substrate in contact with the silica layer. Fig. S1 of the supplementary materials reveals a sharp interface with a thickness of around 8 nm. Fig. S2 of the supplementary materials develops the interface characterization in the point of view of the Si and SiO_2 phases distribution thanks to EELS spectrum-imaging. This study reveals that the deposited SiO_2 film is very homogeneous through the layer excepted for the first deposited nanometers where the mixing between Si and SiO_2 phases is observed on a thin layer of 2 nm. Fig. 2c shows a STEM-HAADF high-resolution image in mean atomic number ($\overline{Z}$) contrast imaging mode. Considering that $\overline{Z} = 10.4$ for the SiO_2 layer and 14.0 for the Si substrate, the SiO_2 film appears darker than the heavier Si substrate. The fast Fourier transform (FFT) of the film in the upper insert confirms its amorphous nature with no specific diffraction point. The dumbbells of Si in the substrate are visible in the high-resolution STEM-HAADF image, and the FFT pattern observed in the lower insert reveals an orientation according to the [110] direction.

Elementary concentration profiles were obtained by XPS on the same film deposited at 500 °C, after sputtering with Ar_{500+} clusters. The obtained depth profile of Fig. 2d shows a 25 nm thick interface over-estimated by the defect of analysis points in this region. This profile confirms the oxygen diffusion in the substrate at a concentration around 3 at.%. The carbon content reaches 4 at.% in the extreme 10 nm thick superficial layer and is negligible after the first sputtering step, in agreement with the NRA analysis. As a major result, the O/Si ratio is homogeneous beyond the first 10 nm, with an average value of 2.2 ± 0.1. It is worth recalling that sputtering with argon clusters provides these results and especially the oxygen measurement with high reliability. The ToF-SIMS profile of Fig. 2e corresponding to the normalized oxygen ion signal matches the results obtained from XPS. The uniform distribution of silicon and Si_xO_y species and the extremely low carbon contamination in the film are also confirmed by the ToF-SIMS analysis, despite the qualitative character of the technique in these conditions. The EDS analysis of the same film deposited at 500 °C, illustrated by the O and Si profiles in Fig. S1 in supplementary materials, reveals a significant oxygen content at the interfacial layer. This result is in agreement with the XPS ones, highlighting the possible presence of a passivation layer. Along the profile, and taking into account

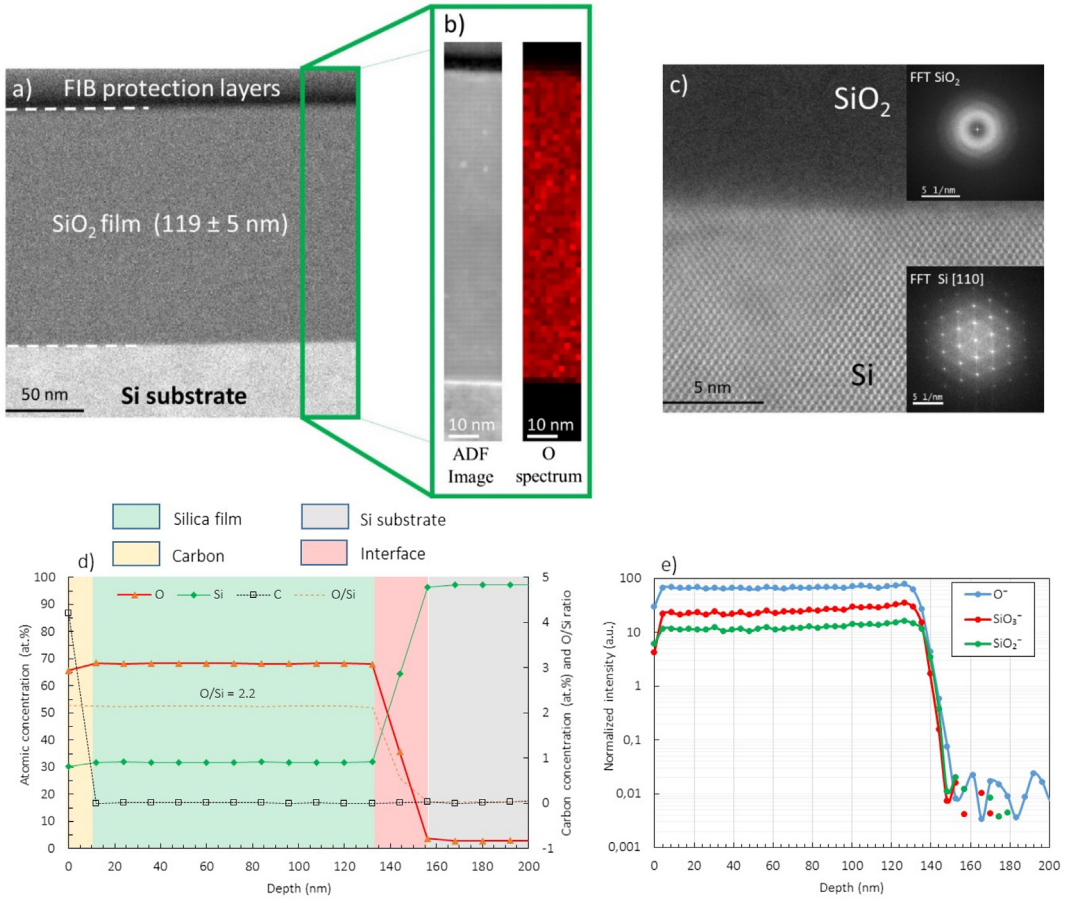

Fig. 2 – a), STEM-HAADF image of a sample deposited at 500 °C showing from the top to the bottom: FIB protection layers (Pt and C), SiO_2 deposited film with the thickness estimation and the silicon substrate. b), Annular Dark Field image and the corresponding oxygen spectrum obtained from EELS spectroscopy. c), High resolution STEM-HAADF image of the sample, including the FFT of the amorphous SiO_2 deposited film and of the crystalline silicon substrate oriented along the [110] direction. d), Si, O, C concentration profiles determined by XPS and the corresponding O/Si atomic ratio. e), O^-, SiO_2^- and SiO_3^- profiles determined by ToF-SIMS.

the uncertainty of the measurements, the oxygen and silicon contents obtained are close to the SiO_2 stoichiometry, except in a 20 nm thick surface layer where a light oxygen deficiency is reported, attributed to the FIB preparation method. High-resolution XPS acquisition was carried out on the same sample. Typical deconvolution of Si2p and O1s symmetric peaks is shown in Fig. S3 of the supplementary material. It reveals a unique component located respectively at 103.7 and 533.1 eV, confirming the Si–O bond corresponding to SiO_2 [39]. Some hydrated Si_xHO_y species are identified as well (Fig. S4 in supplementary material), which are also uniformly distributed in the film with a slight increase in the extreme surface region.

AFM surface maps show a rather smooth surface for all films, independently of their thickness. At $T_d = 500$ °C, an RMS roughness value of 5.0 ± 0.1 nm is measured for a thickness of 134 nm. At the same temperature, a 505 nm thick film presents a slightly lower RMS roughness of 4.7 ± 0.3 nm and also a slightly reduced surface roughness ratio of 25.1 ± 1.1% (compared to 28.6 ± 1.6% for a 134 nm thick film). These results are illustrated in Fig. S4a–b and Table S1 in the supplementary material. The figures reveal rather homogeneous grain size with a maximal topography deviation of 35 nm.

Fig. 3 shows FTIR spectra of the samples deposited at 400, 450, 500 and 550 °C. Six main characteristic vibrational modes are detected from 400 to 4000 cm^{-1} and are identified in the survey spectrum of Fig. 3a. They are assigned to the transverse optical bending mode of the Si–O–Si bond TO_2, the asymmetric stretching of the Si–O–Si bond TO_3 and its corresponding longitudinal optical mode LO_3 due to the TO_3, LO_3 splitting and finally, to the vibration modes of silanol and water molecules [40–43].

Physically adsorbed H_2O is expected to contribute to a band at around 1600 cm^{-1} and in the range 2800–4000 cm^{-1} in sufficiently hydrated samples [42]. Fig. 3b focuses on the spectral range between 2600 and 3800 cm^{-1}, assigned to hydrated species H_2O and silanol. The broad absorption band at around 3400 cm^{-1} dominates the signal for low T_d. This is due to the symmetric and asymmetric OH stretching of molecular water, which is bounded to the silica network [41,44]. The shoulder at around 3200 cm^{-1} is also assigned to asymmetric stretching of molecular water. For the highest T_d values, the spectrum shows some peaks at around 3550, 3600 and 3650 cm^{-1}. These signals are attributed to the OH stretching of silanols, which are hydrogen-bonded to the oxygen of the neighboring silanols and to the neighboring water molecules for 3550 and 3600 cm^{-1}, respectively. The signal at around 3650 cm^{-1} is attributed to the OH stretching of type II (hydrogen-bonded to molecular water which is bound to the silica network) in the glass [42]. The intensity of the 2800–4000 cm^{-1} broad band decreases with increasing T_d and this trend reveals a steeper decrease of the concentration of molecular water than that of silanol groups. The presence of hydrated species is also evidenced by the ERDA measurements (Fig. 3d). The ERDA signal is rather symmetric, indicating a uniform distribution of the hydrated species along the thickness of the film, in agreement with the ToF-SIMS measurements (Fig. S4 – supplementary materials). These ERDA signals were processed to quantify the hydrogen content in function of T_d, as it will be presented in the next section.

The second region in the spectral range 700–1400 cm^{-1} zoomed in Fig. 3c shows four vibration modes. The most intense absorption peak (TO_3) centered at 1050 cm^{-1} confirms the formation of an amorphous SiO_2 network structure in the

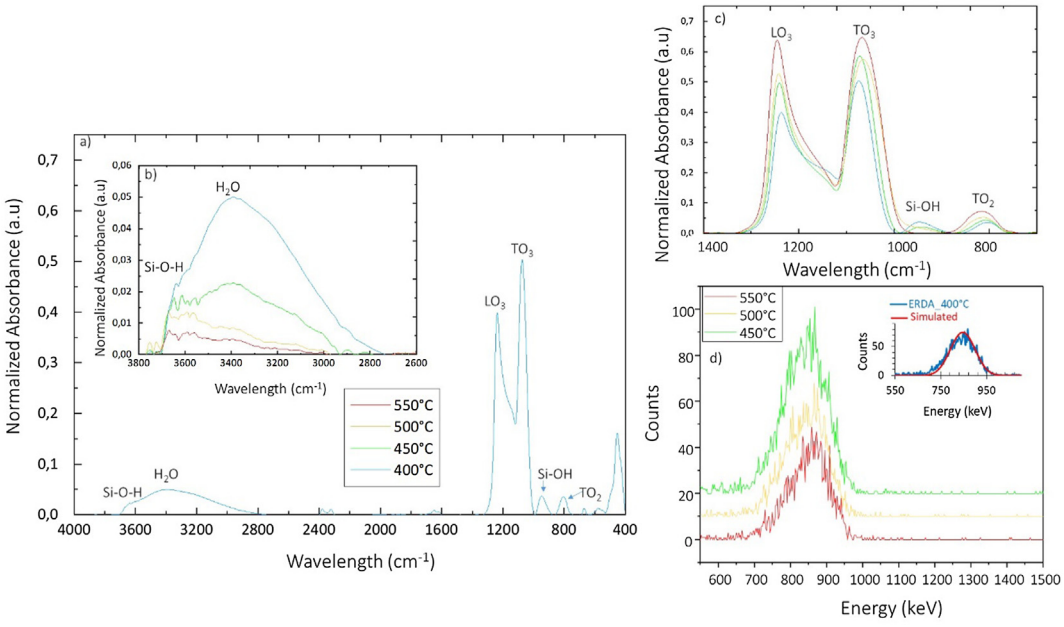

Fig. 3 – a), FTIR spectrum of a SiO_2 film deposited at $T_d = 400$ °C. b), Zoom in the 2600–3800 cm^{-1} range of the FTIR spectra containing Si–OH and H–O–H vibrational modes, for the films processed at different T_d. c), Zoom in the 700–1400 cm^{-1} area of the FTIR spectra for the films processed at different T_d containing the TO_2, Si–OH, TO_3, LO_3 vibrational modes. d), Comparison of ERDA measurements for samples deposited in the temperature range between 450 and 550 °C. Example of ERDA spectrum simulation at 400 °C: black and red curves refer to experimental and simulated results respectively.

film as observed with TEM analysis (Fig. 2c). The vibration mode at around 800 cm^{-1} is assigned to TO_2 Si–O–Si bond and evidences the chemical bond between SiO_4 tetrahedra [45]. The intensity of this vibration mode increases with increasing T_d, revealing an improvement of the medium-range order of the network. The weak vibration mode at around 940 cm^{-1}, not discernible for T_d of 550 °C, is assigned to Si–OH bonds. Silanols are hydrogen-bonded to molecular water [42]. This band is particularly intense in porous silica and silica gels [42], in contrast to the present work. Its intensity decreases with increasing T_d in the same way as the broad band at around 3400 cm^{-1}. TO_3 and LO_3 vibration modes are shifted respectively toward lower and higher frequencies when T_d increases and the vibration mode intensities increase along with it.

The evolution of these vibrations with increasing T_d can be explained by an increase of the population of the Si–O–Si bonds [9]. These results indicate a densification and a polymerization of the silica network when T_d increases, achieved by the reduction of the number of molecular water and OH species that leads to the formation of new Si–O–Si cross-linking bonds. Consequently, the connectivity of Si–O–Si bonds network is improved, evidenced by a shift of TO_2 band towards higher wavenumbers.

3.2. *Chemical composition, hydration species and properties*

Fig. 4 reveals the evolution of the average hydrogen content (at.%) and the O/Si atomic ratio as a function of T_d, determined from the simulation of IBA spectra. The hydrogen content decreases with increasing T_d from 7.8 at.% at 400 °C to 4.5 at.% at 550 °C. The O/Si total atomic ratio remains stable between 400 and 450 °C (1.93 ± 0.01) and it slightly increases above 450 °C to reach 2.24 ± 0.01 at 550 °C. The total hydrogen content being known from IBA, FTIR allows assigning the hydrogen distribution in the silica network. As revealed from Fig. 3a, hydrogen in the film is involved in H_2O and OH from silanol groups. Based on this information, the evolution of the O/Si atomic ratio in the Si–O–Si network is corrected by subtracting from the total oxygen content, the atomic percentage of oxygen that is found in hydrogen involving groups as presented in Table S2 of the supplementary materials. We consider two extreme cases where all hydrogen is involved either as molecular H_2O (O/Si**) or as hydroxide group OH (O/Si*). The corrected O/Si atomic ratios for these two cases are also presented in Fig. 4a. At 500 °C, the O/Si* and O/Si** values are equal to 2.0 ± 0.1, the expected value for stoichiometric silica. The raw stoichiometry is very well described by the presence of Q^3(OH) species (silicon tetrahedrally coordinated with 3 bridging oxygen and one hydroxyl) for a part of 16% as discussed in the supplementary materials and Table S2. Taking into account the measurement uncertainties, IBA results are in good agreement with the XPS profile of the film deposited at 500 °C. Indeed, the average O/Si value of 2.2 determined by XPS, corrected for the hydrogen content determined by ERDA, allows to establish the ratio limits O/Si* = 2.0 and O/Si** = 2.1, which are in agreement with the corrected IBA results and confirm the stoichiometry of SiO_2 phase. In accordance with the low H_2O content probed by FTIR, the 2.0 value for the O/Si* ratio could be privileged.

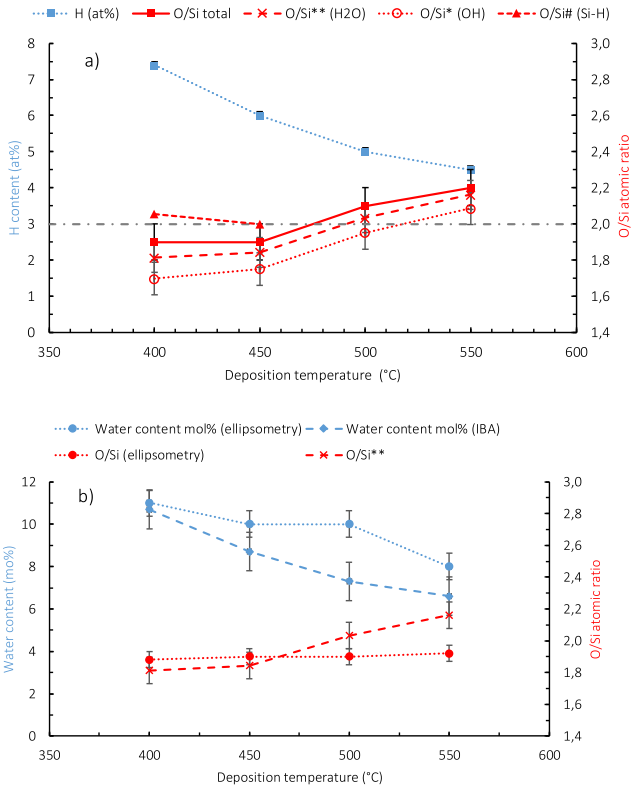

Fig. 4 – a), Evolution of the H content and O/Si total atomic ratio, obtained by coupling RBS, NRA and ERDA results as function of T_d. According to ERDA, corrected O/Si and O/Si* atomic ratios are drawn considering that hydrogen completely involved in the formation of either H_2O or OH silanol groups, respectively. Corrected O/Si# values assume that hydrogen is completely involved in Si–H and H_2O groups at the lowest temperatures (see details Table S2). b) Comparison of the evolution of water content and O/Si atomic ratio determined by IBA and ellipsometry, the later using the BEMA model, as function of T_d.**

Similarly, at 550 °C the O/Si* value calculated from IBA is also in agreement with the stoichiometric silica (2.1 ± 0.1), but the O/Si** remains in slight excess and must be discarded taking into account the FTIR results. Here, the raw stoichiometry is calculated with a deviation of 7% taking into account the presence of Q^3(OH) species for a part of 15% (as discussed Table S2). Moreover, EDS Fig. S1, supplementary material, yields an average O/Si ratio of 2.0 ± 0.3, corresponding to a SiO_2 stoichiometry, in good agreement with the previous results within the accuracy limits for this measurement. At 400 and 450 °C, the presence of H_2O and Si–OH species is not sufficient to explain the IBA results. In agreement with the literature, at low CVD temperature, some Si–H bonds are expected as defects in the film or at the film/Si interface [31]. In the present study, considering a part of hydrogen involved in such bonds and the remaining part involved in H_2O bonds (OH species are not considered for simplification), a SiO_2 network with the expected O/Si ratio of 2 could be deduced from IBA measurements (Fig. 4, Table S2). In this hypothesis, around 9% and 6% of the total silicon would be involved in Si–H bonds at 400 and 450 °C respectively. However, no contribution from Si–H

bonds at the expected value of 2250 cm^{-1} was observed by FTIR [46] in agreement with the low concentration of these hydrogen-related impurities.

In a complementary way, Fig. 4b shows the evolution of the H_2O content and O/Si atomic ratio determined by ellipsometry using BEMA model, with the a-Si component representing the concentration of Si–OH bonds. From the volumetric fractions of SiO_2, Si–OH and H_2O, their respective molar fractions and atomic concentration were derived. The estimated O/Si ratio is close to 2.1 and the H_2O content varies from 11 mol.% at 400 °C to 8 mol.% at 550 °C, confirming the decrease of hydrated species with increasing T_d, in qualitative agreement with IBA results. The deviation between ellipsometry and IBA values is 1–20% for the H_2O content and 6–10% for the O/Si ratio. The BEMA model catches the order of magnitude of hydrogen content as determined by IBA. The observed differences between the two methods are due to the lack in the ellipsometric model of a component attributed to silanol and to the possible presence of nanoporosity in the film processed at the lower T_d.

Fig. 5a reveals the evolution of the Young's modulus and hardness as a function of T_d. Both parameters remain stable in the investigated T_d range, with average values of 64.2 ± 1.7 and 7.4 ± 0.3 GPa for the elastic Young's modulus and hardness respectively. Fig. 5a also reveals the evolution of the critical load of delamination ($CL_{delamination}$), which is the normal force that a film undergoing a nanoscratch test, starts to delaminate from the substrate. The critical loads were identified by optical microscope and SEM analysis of the scratch track as illustrated in Fig. 5b. At low T_d, $CL_{delamination}$ is rather stable with a slight increase from 10.8 ± 0.1 mN (respective values for the three tests: 10.9/10.8/10.7 mN) at 400 °C to 16.6 ± 1.1 mN at 450 °C (respective values: 17.8/16.3/15.6 mN). A seven fold, sharp increase of $CL_{delamination}$ is observed between 450 and 500 °C (74.2 ± 1.2 mN, respective values: 75.5/73.7/73.3 mN), where the $CL_{delamination}$ reaches a new plateau with a value of 75.1 ± 1.5 mN at 550 °C (respective values: 76.7/74.7/73.8 mN). The micrographs panorama of scratch at T_d = 500 °C, Fig. 5b reveals that the start of the ductile-to-brittle transition occurs for a normal load of 17 mN with tensile hertzian cracking inside the plastic groove of scratch shown Fig. 5b-m1. Then for a load of 42 mN illustrated by the micrograph m2, the localized coating flaking starts: radial chevron and lateral subsurface cracks lead to chipping outside the track. The micrograph m3

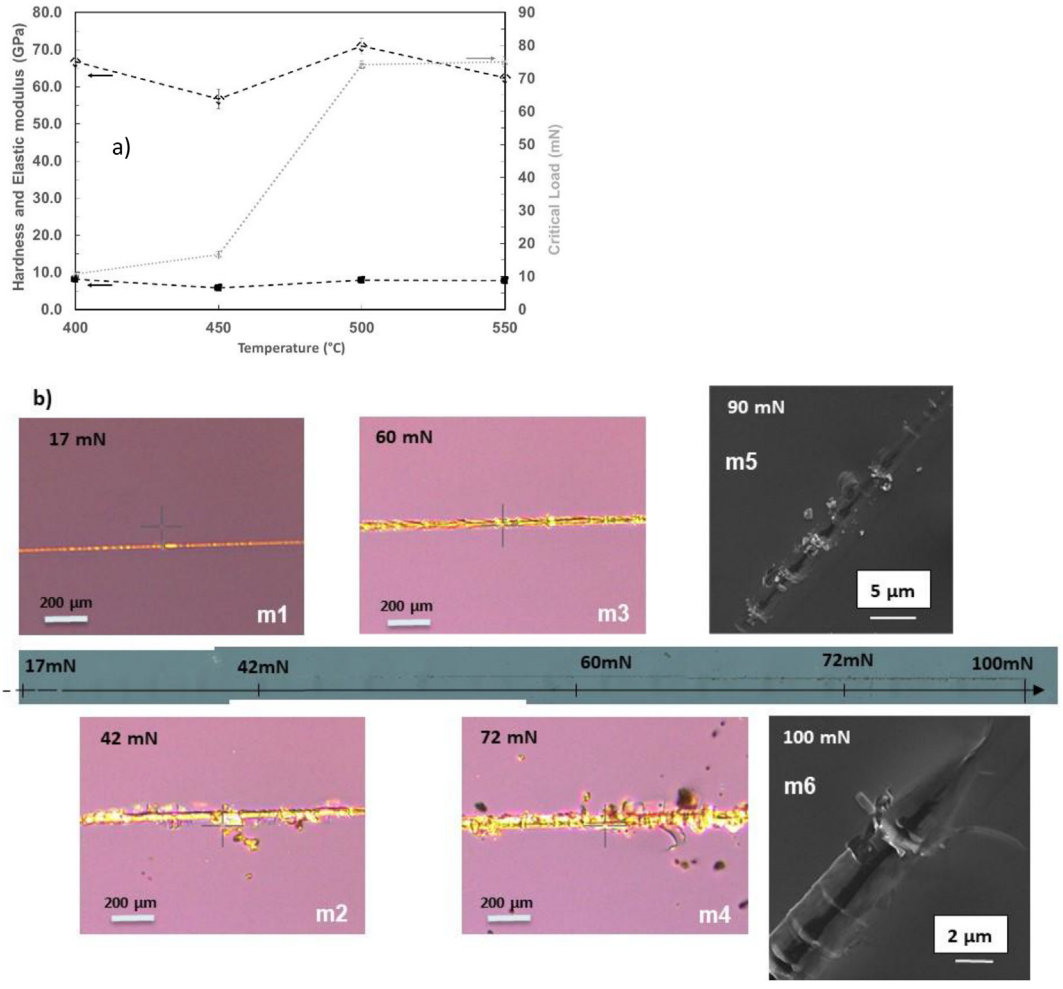

Fig. 5 – a), Evolution of the elastic Young's modulus (black diamonds), hardness (black squares) and critical load of delamination (gray squares) of the films as function of T_d. b), panorama image by optical microscope (m1–4) and secondary electron mode of SEM micrographs (m5–6) of an entire track obtained after the nanoscratch test for T_d = 500 °C.

exhibits these radial and lateral cracks for a load of 60 mN. Finally, the film delamination with larger and continuous chipping occurs for a critical load of 72 mN (Fig. 5b-m4). The micrographs m5–6 show the track with the naked silicon substrate at the highest normal load at the end of the track, the hertzian and chevron cracks inside and along the track and the film chipping inside and outside the track. The significantly higher normal force required to separate the coating from the silicon substrate indicates a stronger adherence when deposited at higher temperatures.

Similarly to Fig. 5, Fig. 6 presents the evolution of the P-etch rate and the contact angle of the films as a function of T_d. The P-etch rate of films deposited at 400 °C is 19 Å/s corresponding to moderate corrosion resistance. The P-etch rate of films deposited at 450 °C is strongly decreased to 11 Å/s and then it only slightly decreases to reach 9 Å/s for films deposited at 550 °C. These results are very comparable to those of Ponton et al. [9] obtained from CVD SiO_2 from TEOS/O_2 in a similar temperature range. For comparison, the P-etch rate of films elaborated at lower temperatures by atmospheric CVD varies in a similar range, from 17.3 at 125 °C to 6.6 Å/s at 250 °C, with a strong evolution of the deposition rate between 5 and 20 nm/min in this temperature range [47].

At the same time, the water contact angle confirms the hydrophilic character of the silica surface without, however, the same intensity along the investigated T_d range. The water contact angle moderately increases from 53 ± 1 to 63 ± 1° when T_d is increased from 400 to 500 °C. Further increase of T_d to 550 °C results in a slight decrease of the contact angle (57 ± 1°). These results are similar to those previously reported for SiO_2 films synthesized from sol–gel dip coating using TEOS as silicon source and heat treated at 250 °C (58° for a RMS roughness of 3.65 nm) [48]. In their study, S. Choudhary et al. [48] attributed the stronger wetting to more numbers of hydroxyl groups at the surface and to the roughness.

4. Discussion

The deposited silica films are amorphous, homogeneous, non-textured and non-porous in the entire temperature range of 400–550 °C, with a clear and narrow interface with the silicon substrate. They contain molecular water and silanol groups,

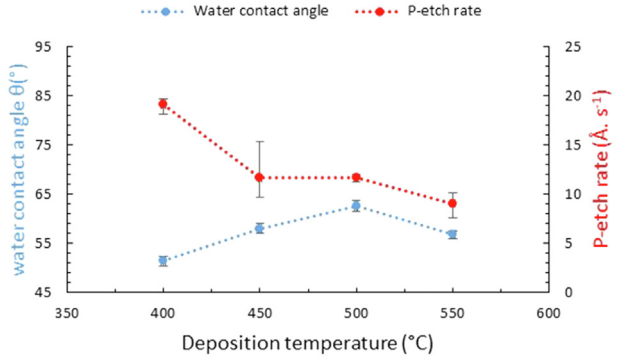

Fig. 6 – P-etch rate and pure water contact angle of the deposited films as a function of the T_d between 400 °C and 550 °C.

especially at the lowest temperatures. At these temperatures, the $O^{\cdot}$ radicals, produced from the thermal decomposition of O_3 [30], react with TEOS to promote the substitution of ethyl ($-C_2H_5$) side groups by hydroxyl (–OH) ones. At higher temperatures, intermediate species such as $Si(OH)(OC_2H_5)_3$ are produced from the oxidation of TEOS in the gas phase [28]. In these conditions, the formation of pure SiO_2 is privileged by a condensation-dehydration mechanism involving two Si–OH moieties –[30]:

$$-Si-OH(surface) + -Si-OH(gas\ phase\ intermediate) \rightarrow Si-O-Si(s) + H_2O \quad (2)$$

It is noticeable that the water content decreases more sharply with increasing T_d than that of silanol groups according to the evolution of the high frequency FTIR signal in the range 2800–4000 cm^{-1}. Additionally, no peak corresponding to Si–OH bonds is seen at 940 cm^{-1} above $T_d = 500$ °C confirming the absence of hydrated nanoporosities, which has also been verified by refractive index measurements (not presented). It thus appears that the hydrated species in the films intrinsically depend on the deposition process. In agreement with the presented results, it is well known that the thermal treatment of silicate glasses and silica allows eliminating a large part of H_2O and vicinal silanols, driving to a reduction of the broad 2800–4000 cm^{-1} IR band [42,49]. It was shown that FTIR spectra of silica samples heat treated at 700 °C contain free silanols (3747 cm^{-1}), exclusively [49]. Also, Zhuravlev and Potapov [50] showed that, when colloidal silica is heat treated in the range 200–400 °C, internal hydrated species are slowly removed. Removal of such species is accelerated at 400–600 °C and reveals the diffusion role on the transport of the condensation products. Hydroxyl groups completely disappear after heat treatment in the range 900–1000 °C [50]. In the present study, the TO_3/LO_3 splitting testifies the presence of short and/or medium-range order of the SiO_4 tetrahedra network [45]. No such splitting is expected in a completely random network. The more the distance between the two peaks (TO and LO) increases, the more the silica network structure exhibits medium-range order [43,45,51]. In the present work, LO_3 is shifted towards higher wavenumbers and TO_3 is shifted toward lower wavenumbers when T_d increases. These results indicate that the Si–O–Si network is better ordered and polymerized with the increase of T_d, because of the prevailing dehydration mechanisms. Indeed, the decrease content of H_2O and OH species results in the formation of new Si–O–Si cross-links with subsequent evolution of the SiO_2 structure towards a more polymerized, dense and rigid network.

The present work also reveals that the H content of the films, along with their O/Si ratio, depends on T_d. It is recalled that the H content drops gradually from 7.4 at.% at 400 °C to 4.5 at.% at 550 °C and at the same time the raw O/Si average ratio increases from 1.93 to 2.24, corresponding to 85% of stoichiometric 2.0 ± 0.1 silica from T_d = 500 °C, when excluding the part of oxygen atoms involved in silanol groups. The slight oxygen deficiency observed below 450 °C has already been reported in the literature for thermal CVD process from TEOS chemistry and assigned to the presence of hydrogen-related impurities and trapped charges highlighted

notably by leakage – current density or relative dielectric constant measurements [31,52]. Here, a very low amount of Si–H bonds (lower than 10% of the total silicon) could be an element of explanation to interpret this global oxygen deficiency. As mentioned, the carbon content of the relatively thin 100–150 nm films is remarkably low (below the detection limit of NRA and EELS), highlighting the effect of O_3 and O_2 in ensuring such purity through the activity of $O^{\cdot}$ radicals. As suggested by Nishiguchi et al. [31], the oxygen atoms are able to diffuse in the film and passivate weak bonds (such as Si–Si dangling bonds, Si–C, Si–OH, Si–H, etc.). Fig. S6 shows results on 505 nm thick films obtained at $T_d = 500$ °C that reveals also a very stable raw O/Si value (O/Si = 2.1), an absence of carbon and also of oxygen enrichment in the substrate unlike the thinner film. This observation suggests a lower oxygen diffusion induced by the deposited thickness. The O/Si corrected ratio for both films is consistent with that of a stoichiometric silica. The diffusion of oxygen atoms and radicals is associated with the oxidizing mechanisms of carbon or hydrogen involving weak bonds and participates to the removal of these oxidized species. This mechanism is accentuated with increasing T_d and acts on the O/Si stoichiometry and on the carbon content. For the thickest films, the diffusion could also depend on the deposition rate, with higher deposition rates resulting in less efficient diffusion.

Similar decrease of the hydrated species with increasing T_d was observed by Ponton et al. [9] for silica films deposited by thermal CVD from TEOS and O_2. Fig. 7 compares FTIR survey spectra of films deposited from the two chemistries at T_d 550 and 400 °C. The H_2O content is significantly lower for the films deposited from TEOS/O_2/O_3. Indeed, for these films, the relative area of 2800–4000 cm^{-1} band is reduced by a factor of 1.5 at 400 °C and 10 at 550 °C comparably to those deposited from TEOS/O_2. We conclude that the participation of O_3 in the reactive gas strongly enhances the dehydration and condensation mechanisms through the formation of siloxane bonds in the Si–O–Si network. A favorable effect of the O_2–O_3 combination is also probable taking into account the very low hydrated species and carbon content of the films in the present work compared to films obtained from CVD using O_2 as oxidant. The TEOS/O_2/O_3 chemistry could benefit from multiple homogeneous chemical reactions, with the simultaneous contribution of O_2, O_3 or $O^{\cdot}$ to the oxidation of intermediated species generated by the decomposition of TEOS. The films present low carbon and hydrated species contents at a given T_d with their structural and chemical characteristics being closer to those of pure silica.

The reduction of the hydrophilic character of the films, observed for the highest T_d (water contact angles 53 and 63° at 400 and 500 °C, respectively) is coherent with the reduction of the hydrated species revealed by ERDA and FTIR. Indeed, the dehydration processes and the nature of hydroxyl bonds at the surface directly impact the contact angle. According to Hair and Hertl [53], free OH groups at the surface of silica reduce the affinity to water, as opposed to hydrogen bonded hydroxyl groups on which water can readily physisorb. It is worth nothing that the contact angle measured for as-received fused silica (SQ-1 SCHOTT®, hydroxyl content 1200 ppm) [54] is 81 ± 8° [55]. This value can be considered as a maximum for such silica with a high IR component at 3750 cm^{-1} assigned to free OH groups [55]. In the present case, a low intensity at 3750 cm^{-1} was detected for films conditioned in air and explains their higher hydrophilic character.

The Young's modulus, an intrinsic material property, is intimately correlated with the type of bonds existing in the material. As such, its value can be discussed as a function of the composition, the microstructure and stiffness of the network [56–59]. The commonly accepted values of elastic Young's modulus and hardness for SiO_2 glass are in the range of 65–73 GPa [37,60,61] and 5–8 GPa respectively [37,62]. Rouxel [10] has concluded to the prevalence of two major parameters to describe the elastic moduli behavior of glasses, such as the interatomic bonding energy (Si–O bonds have a very high energy of 800 kJ/mol) and the atomic packing density (0.45 for amorphous silica), with a predominating influence of the last one.

The values of 64.2 ± 1.7 and 7.4 ± 0.3 GPa for the elastic modulus and the hardness respectively, determined for the present thick films, where the bias due to the influence of the substrate and of the defects of the indenter apex is minimized, lie in the lower range of the literature data for the silica glass [37,61]. Some previous works have revealed the sensitivity of hardness tests to the glass surface alteration with water related to the formation of silanol groups in severe conditions [62–64].

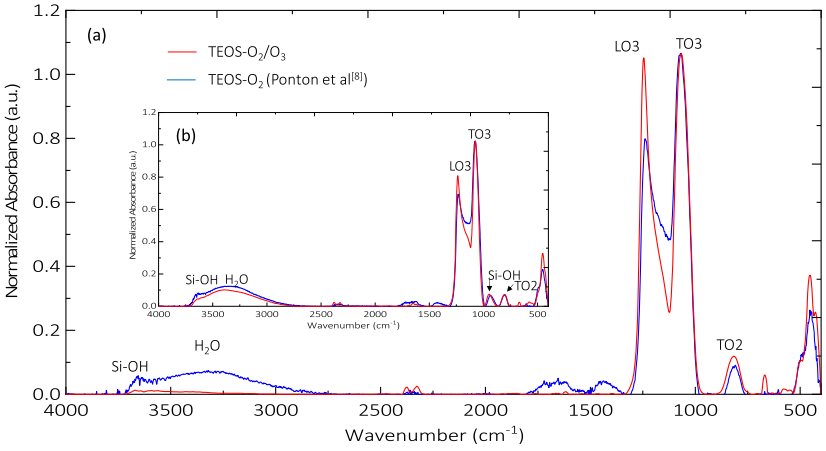

Fig. 7 – Comparison of FTIR spectra of films deposited with TEOS-O_2 and TEOS-O_2-O_3 at T_d of, a: 550 °C and b: 400 °C [8].

The Young's modulus has also been shown to decrease with increasing hydrated species content [65]. The simulation conducted by Mei et al. [66] allows to determine the respective water effect on the silica glass mechanical properties: on the one hand of molecular water and on the other hand of silanol hydroxyl groups. If the introduction of molecular water leads to a moderate increase of Young's modulus of silica glass, the introduction of hydroxyl groups, reducing the network connectivity, exhibits a stronger decrease of about 25% for 18.5 mol.% of water introduced. In the present work, the very low hydrated species content differences (3.3 at.% of hydrogen between 450 and 550 °C) detected in the range 450–550 °C and the presence of both molecular water (<6.5 mol.%) and silanol groups (15 ± 1% of Si–OH bonds at 500 and 550 °C) within the glass coating, as highlighted by FTIR in Figs. 3 and 7, lead to limited but antagonist effects resulting in the relative stability of Young's modulus and hardness within this content range.

The improved adhesion to the silicon substrates of the films deposited at T_d above 450 °C underlies a relation between the critical load of delamination and the physicochemical characteristics of the films. As previously described, the films deposited at 400 and 450 °C are slightly substoichiometric and their content in hydrogen-related impurities and weak bonds is probably higher. It is likely that the silicon substrate oxidation occurring at higher temperature and resulting in an oxygen enrichment of the silicon substrate as shown in Fig. 2, benefits to the film adhesion by increasing the Si–O strong bonding network at the interface. A similar annealing effect of ozone on SiO_2 film has been shown by Nishiguchi et al. [31]. Then, the temperature could have an impact on the oxygen diffusion and the passivation of weak bonds located at the interface film/substrate.

The P-etch test applied in the present work involves interaction of the silica network with polymeric HF aqueous species $H_nF_{n+1}^-$ resulting from the solvation of F^- by molecular HF [17]. Silica dissolution requires the breaking of all four siloxane bonds of each tetrahedron unit to release each silicon atom from the network and create Si–F bonds successively, with this substitution reaction rate being pH dependent. Literature results indicate that the etching rate of SiO_2 is not a simple function of the HF concentration [17,67–69], and may depend on an adsorption mechanism of HF and/or HF_2^- on silanol groups and silicon atoms with a catalytic effect of H_2O or H^+ [70,71]. Mitra and Rimstidt [16] introduced an empirical dissolution rate law, Eq. (3), for amorphous silica deduced from a compilation of literature data. They concluded that the rate-determining step for silica dissolution in fluoride solutions involves a coordinated attack of a Lewis acid, on the bridging O atom and a Lewis base on the Si atom, potentially H^+ and HF_2^-. A precursor step for the bond breaking is the adsorption of the reacting species onto the silica surface.

$$r(mol/m^2s) = 10^{0.48} e^{\frac{-34243}{RT}} a_{HF}^{1.50} a_{H^+}^{-0.46} \quad (3)$$

where $10^{-2.37} < a_{HF} < 10^{1.61}$ (a_{HF}: HF chemical activity), $-0.32 < pH < 4.76$ and $296 < T < 343$ K. According to Eq. (3), the expected etching rate corresponding to the present chemical conditions is around 4 Å/s. The obtained etching rate at 400 °C is relatively high and strongly drops at 550 °C (19 vs 9 Å/s). These values remain above the predicted value from the rate law equation established by Mitra and Rimstidt [16]. In order to elucidate this discrepancy, we carried out two additional experiments. They consisted in depositing a film at 400 °C and another at 550 °C, following by a 2 h annealing at 550 °C under N_2 flow. For these films, the etching rate measured after annealing is 4.2 ± 0.3 and 4.0 ± 0.1 Å/s, respectively, in excellent agreement with the one of 4 Å/s proposed by the model of Mitra and Rimstidt [16]. We can conclude that this thermal treatment allows dehydration and network polymerization in the films. Indeed, we showed for the as-processed films that the hydrated species are located at the surface and in the bulk as retained silanols or bound water in the skeleton. The major mechanism of dehydration consists in the silanols condensation reaction with the removal of a water molecule. Zhuravlev and Potapov [50] showed that the distribution of OH groups between the surface and bulk of silica samples depends on the temperature. Within 200–400 °C, internal water is slowly removed while surface hydrated species rapidly decrease. Above 400 °C, the rate of internal water removal increases when for surface species, this decrease slows down due to the disappearance of surface vicinal silanol groups. Hydrated species are removed by the transport of water molecules from the bulk of the film to the surface, enhanced by the diffusion rate that increases with the temperature. In the present work, despite an almost two times higher content in hydrated species in the sample deposited at 400 °C compared to the one at 550 °C, the post annealing at 550 °C allows finalizing in both samples the condensation reactions and the removal in a very large part, for the surface and internal hydrated species.

Fig. S7 of the supplementary materials compares the FTIR spectra for the as-deposited films at T_d 400 and 550 °C and the annealed film deposited at 400 °C. The annealing strongly reduces the high frequency band relative to the hydrated species up to an intensity similar to this of the film deposited at 550 °C. Despite the observed structural similarities, the global quality of the annealed film structure stays slightly lower than this for the film deposited at 550 °C. The investigated thermal treatment is efficient to remove a large part of water and silanol species but the condensation reactions are not complete in the absence of oxidant agent. Nonetheless, the etching rate is lower for this annealed sample compared to the sample deposited at 550 °C that could be explained by the surface reactivity of such un-annealed film.

Further investigation of these dehydration mechanisms correlated to the surface and network polymerization may be performed through complementary coupled measurements of etching rate and nanoindentation on films that have been etched for longer durations, and by using deuteron-exchange with heavy water D_2O in the etching solution.

5. Conclusion

A comprehensive description of SiO_2 films deposited by atmospheric pressure thermal CVD from TEOS-O_2/O_3 has been carried out in the 400–550 °C deposition temperature range. Compared to TEOS/O_2 CVD chemistry, the use of O_2/O_3 gas as oxidant increases the oxidation potential through additional homogeneous reactions, beneficial to TEOS oxidation, with a

remarkable low content in hydrated species and carbon. The presence of ozone allows increasing the structural and chemical quality of SiO_2 films. These physical and chemical characteristics depend on the deposition temperature. The influence of the latter on the content of hydrated species was accurately quantified, and allowed deducing a reliable O/Si value along depth profiles. Above 450 °C the SiO_2 films reveal a stoichiometry O/Si = 2.1 ± 0.1 in agreement with a low content of hydrated species (less than 5 at.% of hydrogen). Below 450 °C, the hypothesis of Si–H weak bonds (<9% of the total silicon) and water molecules is proposed to explain a slight sub-stoichiometry (O/Si = 1.93 ± 0.01). The dehydration processes and the enhancement of the network rigidity by the creation of new Si–O–Si cross-linking are closely related, and together they reveal a molecular or medium-range order network ordering with increasing T_d. Nanoindentation tests confirmed the chemical and structural quality of the films, attesting on the low contribution of the hydrated species or impurities on the interatomic bonding energy and the molecular organization. Despite the low variation of the hardness and Young's modulus within the investigated deposition temperature range, the critical load of delamination strongly increases with increasing the deposition temperature in relation with the film/substrate interface quality and the silicon substrate oxidation extended over a few nanometers. The results of P-etch tests revealed a strong dependency on the network organization and hydration. The measured etching rates for annealed films (4.0 ± 0.1 Å/s) are in excellent agreement with the rate law equation proposed by Mitra and Rimstidt [16] for silica.

The multiple characterizations carried out show that the films deposited at 500 °C and above are potentially of the greatest interest, combining both the best chemical and structural properties and good mechanical and etching performances.

In the end, the wealth of the complementary characterization techniques implemented here, not only confirmed the major mechanisms involved in the synthesis of silica, but has also consolidated the description of the system in terms of temperature and oxidant gas, by providing structural, physical and chemical quantitative data relevant to the silica film in the range 400–550 °C. These trends and results can be used later as a background for similar materials, e.g. aluminum oxides or silicon oxynitrides.

Statement of contribution

Babacar Diallo designed the study, analyzed the experimental data and wrote the paper. Konstantina Christina Topka performed CVD, FTIR, ellipsometry and P-etch experiments and contributed to the analysis of the results assisted by Diane Samélor. Hélène Lecoq performed IBA experiments supervised by Thierry Sauvage. Cécile Genevois and Mathieu Allix performed the TEM experiments. Charlotte Debesgue, Maxime Puyo and Raphael Laloo performed the nanoscratches and nanoindentation experiments supervised by Viviane Turq. Olivier Debieu performed and supervised ellipsometry measurements and analysis. Brigitte Caussat, Hugues Vergnes, Marie-Joelle Menu, Pierre Florian, François Senocq and Vincent Sarou-Kanian contribute to the results' analysis and their interpretation. Nadia Pellerin and Constantin Vahlas supervised this study included in ANR HEALTHYGLASS project and all the authors helped on paper editing.

Declaration of Competing Interest

The authors declare that they have no known competing financial interests or personal relationships that could have appeared to influence the work reported in this paper.

Acknowledgments

The present work was funded by the French Agence Nationale de la Recherche (ANR) under the Contract HEALTHYGLASS ANR-17-CE08-0056. It was co-funded by the European Union, the Région Centre-Val de Loire and The French Minister of Research (MESRI-DRRT). The authors are indebted to Elodie Chauvet and Charbel Roukoss from TESCAN Analytics for the AFM, XPS and ToF-SIMS measurements, Claudie Josse from the French 'Centre de Microcaratérisation Raymond Castaing', Toulouse, for the FIB preparations of the films, and Simon Ponton (CIRIMAT) and Domingos de Sousa Meneses (CNRS-CEMHTI) for their guidance in IR-spectroscopy analysis and interpretation.

Appendix A. Supplementary data

Supplementary data to this article can be found online at https://doi.org/10.1016/j.jmrt.2021.04.067.

REFERENCES

[1] Li S, Xu J, Wang L, Yang N, Ye X, Yuan X, et al. Effect of post-deposition annealing on atomic layer deposited SiO_2 film for silicon surface passivation. Mater Sci Semicond Process 2020;106:104777.
[2] Dimaria DJ, Dong DW. High current injection into SiO_2 from Si rich SiO_2 films and experimental applications. J Appl Phys 1980;51:2722–35.
[3] Hughes RC. Hole mobility and transport in thin SiO_2 films. Appl Phys Lett 1975;26(8):436–8.
[4] Shefiu K, Yi X, Tan L, Yanxi D, Tsiwah EA, Ahmed ASA, et al. Base-catalyzed synthesis of superhydrophobic and antireflective films for enhanced photoelectronic applications. J Mater Res Technol 2020;9(3):3958–66.
[5] Shi L, Yuan Y, Liang XF, Xia YD, Yin J, Liu ZG. Microstructure and dielectric properties of La_2O_3 doped amorphous SiO_2 films as gate dielectric material. Appl Surf Sci 2007;253:3731–5.
[6] Zhao J, Mao DS, Lin ZX, Jiang BY, Yu YH, Liu XH, et al. Intense short-wavelength photoluminescence from thermal SiO_2 films co-implanted with Si and C ions. Appl Phys Lett 1998;73:1838–40.
[7] Grüniger A, Von Rohr PR. Deposition of SiO_2-like diffusion barriers on PET and paper by PECVD. Surf Coat Technol 2003;174–175:1043–7.
[8] Chen X, Wang YW, Liu X, Wang XB, Zhao YQ. Study of structural and electronic properties of the silanone group as

bulk defect in amorphous SiO_2. J Non-Cryst Solids 2015;414:1–6.
[9] Ponton S, Dhainaut F, Vergnes H, Samelor D, Sadowski D, Rouessac V, et al. Investigation of the densification mechanisms and corrosion resistance of amorphous silica films. J Non-Cryst Solids 2019;515:34–41.
[10] Rouxel T. Elastic properties and short-to medium-range order in glasses. J Am Ceram Soc 2007;90(10):3019–39.
[11] Abrajano TA, Bates JK, Byers CD. Aqueous corrosion of natural and nuclear waste glasses I. Comparative rates of hydration in liquid and vapor environments at elevated temperatures. J Non-Cryst Solids 1986;84:251–7.
[12] Grambow B, Müller R. First-order dissolution rate law and the role of surface layers in glass performance assessment. J Nucl Mater 2001;298:112–24.
[13] Frugier P, Chave T, Gin S, Lartigue JE. Application of the GRAAL model to leaching experiments with SON68 nuclear glass in initially pure water. J Nucl Mater 2009;392:552–67.
[14] Jantzen CM, Brown KG, Pickett JB. Durable glass for thousands of years. Int J Appl Glass Sci 2010;1:38–62.
[15] Osseo-Asare K. Etching kinetics of silicon dioxide in aqueous fluoride solutions : a surface complexation model. J Electrochem Soc 1996;143:1339–47.
[16] Mitra A, Rimstidt JD. Solubility and dissolution rate of silica in acid fluoride solutions. Geochem Cosmochim Acta 2009;73:7045–59.
[17] Spierings GACM. Wet chemical etching of silicate glasses in hydrofluoric acid based solutions. J Mater Sci 1993;28:6261–73.
[18] Liang DT, Readey DW. Dissolution kinetics of crystalline and amorphous silica in hydrofluoric-hydrochloric acid mixtures. J Am Ceram Soc 1987;70:570–7.
[19] Sittinger V, Höfer M, Harig T, Justianto M, Thiem H, Vergöhl M, et al. Optical grade SiO_2 films prepared by HWCVD. Surf Coat Technol 2018;336:61–6.
[20] Ning C, Mingyan L, Weidong Z. Fouling and corrosion properties of SiO_2 coatings on copper in geothermal water. Ind Eng Chem Res 2012;51:6001–17.
[21] Gebhard M, Mai L, Banko L, Mitschker F, Hoppe C, Jaritz M, et al. PEALD of SiO_2 and Al_2O_3 thin films on polypropylene: investigations of the film growth at the interface, stress, and gas barrier properties of dyads. ACS Appl Mater Interfaces 2018;10(8):7422–34.
[22] Esro M, Kolosov O, Jones PJ, Milne WI, Adamopoulos G. Structural and electrical characterization of SiO_2 gate dielectrics deposited from solutions at moderate temperatures in air. ACS Appl Mater Interfaces 2017;9(1):529–36.
[23] Jung H, Kim WH, Oh IK, Lee CW, Lansalot-Matras C, Lee SJ, et al. Growth characteristics and electrical properties of SiO_2 thin films prepared using plasma-enhanced atomic layer deposition and chemical vapor deposition with an aminosilane precursor. J Mater Sci 2016;51:5082–91.
[24] Kim DH, Lee HJ, Jeong H, Shong B, Kim WH, Park TJ. Thermal atomic layer deposition of device-quality SiO_2 thin films under 100 °C using an aminodisilane precursor. Chem Mater 2019;31:5502–8.
[25] Simurka L, Čtvrtlík R, Tomaštík J, Bektas G, Svoboda J, Bange K. Mechanical and optical properties of SiO_2 thin films deposited on glass. Chem Pap 2018;72:2143–51.
[26] Topka KC, Chliavoras GA, Senocq F, Vergnes H, Samelor D, Sadowski D, et al. Large temperature range model for the atmospheric pressure chemical vapor deposition of silicon dioxide films on thermosensitive substrates. Chem Eng Res Des 2020;161:146–58.
[27] Nitodas SF, Favvas EP, Romanos GE, Papadopoulou MA, Mitropoulos AC, Kanellopoulos NK. Development and characterization of silica-based membranes for hydrogen separation. J Porous Mater 2008;15:551–7.
[28] Erlat AG, Wang BC, Spontak RJ, Tropsha Y, Mar KD, Montgomery DB, et al. Morphology and gas barrier properties of thin SiOx coatings on polycarbonate: correlations with plasma-enhanced chemical vapor deposition conditions. J Mater Res 2000;15:704–17.
[29] Skuja L, Kajihara K, Hirano M, Hosono H. Oxygen-excess-related point defects in glassy/amorphous SiO_2 and related materials. Nucl Instrum Methods Phys Res B 2012;286:159–68.
[30] Horita S, Jain P. Dependences of deposition rate and OH content on concentration of added trichloroethylene in low-temperature silicon oxide films deposited using silicone oil and ozone gas. Jpn J Appl Phys 2018;57(3S1). 03DA02-7.
[31] Nishiguchi T, Saito S, Kameda N, Kekura M, Nonaka H, Ichimura S. Improvement in chemical-vapor-deposited-SiO_2 film properties by annealing with UV-light-excited ozone. Jpn J Appl Phys 2009;48:116509. 1-5.
[32] Ponton S, Vergnes H, Samelor D, Sadowski D, Vahlas C, Caussat B. Development of a kinetic model for the moderate temperature chemical vapor deposition of SiO_2 films from tetraethyl orthosilicate and oxygen. AIChE J 2018;00:1–9.
[33] Mayer M. SIMNRA, a simulation program for the analysis of NRA, RBS and ERDA. AIP Conf Proc 1999;475:541–4.
[34] Debarsy PL, Terwagne G. Pure hydrogen references synthesized by low energy ion implantation into amorphous silicon. Nucl Instrum Methods Phys Res B 2019;442:47–52.
[35] Angeli F, Jollivet P, Charpentier T, Fournier M, Gin S. Structure and chemical durability of lead crystal glass. Environ Sci Technol 2016;50:11549–58.
[36] Tsu DV, Lucovsky G, Davidson BN. Effects of the nearest neighbors and the alloy matrix on SiH stretching vibrations in the amorphous SiOr:H (0<r<2) alloy system. Phys Rev B 1989;40:1795–805.
[37] Oliver WC, Pharr GM. An improved technique for determining hardness and elastic modulus using load and displacement sensing indentation experiments. J Mater Res 1992;7:1564–83.
[38] Pliskin WA. Comparison of properties of dielectric films deposited by various methods. J Vac Sci Technol 1977;14:1064–81.
[39] Koshizaki N, Umehara H, Oyama T. XPS characterization and optical properties of Si/SiO_2, Si/Al_2O_3 and Si/MgO co-sputtered films. Thin Solid Films 1998;325:130–6.
[40] Taraskin SN, Elliott SR. Nature of vibrational excitations in vitreous silica. Phys Rev B 1997;56:8605–22.
[41] Nakashima S, Ohki S, Ochiai S. Infrared microspectroscopy analysis of the chemical state and spatial distribution of hydrous species in minerals. Geochem J 1989;23:57–64.
[42] Davis K, Tomozawa M. An infrared spectroscopic study of water-related species in silica glasses. J Non-Cryst Solids 1996;201:177–98.
[43] Naji M, De Sousa Meneses D, Guimbretière G, Vaills Y. In situ high-temperature probing of the local order of a silicate glass and melt during structural relaxation. J Phys Chem C 2015;119:8838–48.
[44] Aines RD, Rossman GR. Water in minerals? A peak in the infrared. J Geophys Res Solid Earth 1984;89:4059–71.
[45] De Sousa Meneses D, Eckes M, del Campo L, Santos CN, Vaills Y, Echegut P. Investigation of medium range order in silicate glasses by infrared spectroscopy. Vib Spectrosc 2013;65:50–7.
[46] Davis K, Tomozawa M. Water diffusion into silica glass: structural changes in silica glass and their effect on water solubility and diffusivity. J Non-Cryst Solids 1995;185:203–20.

[47] Juárez H, Pacio M, Díaz T, Rosendo E, Garcia G, García A, et al. Low temperature deposition: properties of SiO_2 films from TEOS and ozone by APCVD system. In: The Journal of Physics: Conference Series, organizer. XIX Latin American Symposium on Solid State Physics; 2008 Oct 5-10; Puerto Iguazu, Argentina. IOP Publishing; vol. 167 012020. p. 1–6.
[48] Choudhary S, Singh M, Kale RK. Surfactant-catalyzed SiO_2 thin films preparation and characterization. J Adhes Sci Technol 2013;27:2629–41.
[49] Gallas J, Lavalley J, Burneau A, Barres O. Comparative study of the surface hydroxyl groups of fumed and precipitated silicas. 4. Infrared study of dehydroxylation by thermal treatments. Langmuir 1991;7:1235–40.
[50] Zhuravlev LT, Potapov VV. Density of silanol groups on the surface of silica precipitated from a hydrothermal solution. Russ J Phys Chem 2006;80(7):1119–28.
[51] Benitez F, Martinez E, Esteve J. Improvement of hardness in plasma polymerized hexamethyldisiloxane coatings by silica-like surface modification. Thin Solid Films 2000;377–378:109–14.
[52] Vallée C, Goullet A, Nicolazo F, Granier A, Turban G. In situ ellipsometry and infrared analysis of PECVD SiO_2 films deposited in an O_2/TEOS helicon reactor. J Non-Cryst Solids 1997;216:48–54.
[53] Hair ML, Hertl W. Adsorption on hydroxylated silica surfaces. J Phys Chem 1969;73:4269–76.
[54] Lithotec Schott. Synthetic fused silica—optical and technical grades. Schott Litothec Fused_silica_us.pdf, https://www.jmcglass.com/down/fused_silica_us.pdf.
[55] DeRosa RL, Schader PA, Shelby JE. Hydrophilic nature of silicate glass surfaces as a function of exposure condition. J Non-Cryst Solids 2003;331:32–40.
[56] Sorarù GD, Dallapiccola E, D'Andrea G. Mechanical characterization of sol–gel-derived silicon oxycarbide glasses. J Am Ceram Soc 1996;79:2074–80.
[57] Sorarù GD, Modena S, Guadagnino E, Colombo P, Egan J, Pantano C. Chemical durability of silicon oxycarbide glasses. J Am Ceram Soc 2002;85:1529–36.
[58] Suyal N, Krajewski T, Mennig M. Sol-gel synthesis and microstructural characterization of silicon oxycarbide glass sheets with high fracture strength and high modulus. J Sol-Gel Sci Technol 1998;13:995–9.
[59] Li H, Bradt RC. The indentation load/size effect and the measurement of the hardness of vitreous silica. J Non-Cryst Solids 1992;146:197–212.
[60] Comte C, Von Stebut J. Microprobe-type measurement of Young's modulus and Poisson coefficient by means of depth sensing indentation and acoustic microscopy. Surf Coat Technol 2002;154:42–8.
[61] Concise encyclopedia of advanced ceramic materials. 1st ed. Brook RJ: Elsevier; 1991.
[62] Scherer K, Nouvelot L, Lacan P, Bosmans R. Optical and mechanical characterization of evaporated SiO_2 layers. Long-term evolution. Appl Opt 1996;35(25):5067–72.
[63] Hirao K, Tomozawa M. Microhardness of SiO_2 glass in various environments. J Am Ceram Soc 1987;70:497–502.
[64] Tomozawa M, Hirao K. Diffusion of water into oxides during microhardness indentation. J Mater Sci Lett 1987;6:867–8.
[65] Ito S, Tomazawa M. Dynamic fatigue of sodium-silicate glasses with high water content. J Phys Colloq 1982;43(C9):611–4.
[66] Mei H, Yang Y, van Duin ACT, Sinnott SB, Mauro JC, Liu L, et al. Effects of water on the mechanical properties of silica glass using molecular dynamics. Acta Mater 2019;178:36–44.
[67] Judge JS. A study of the dissolution of SiO_2 in acidic fluoride solutions. J Electrochem Soc 1971;118(11):1772–5.
[68] Spierings GACM. Review, wet chemical etching of silicate glasses in hydrofluoric acid based solutions. J Mater Sci 1993;28:6261–73.
[69] Prokopowicz-Prigogine M. La réactivité du verre. Le caractère autocatalytique du mecanisme de dissolution de la maille silicique du verre dans un mélange aqueux d'acides fluorhydrique et chlorhydrique. J Chim Phys 1988;85:695–705.
[70] Knotter DM. Etching mechanism of vitreous silicon dioxide in HF-based solutions. J Am Chem Soc 2000;122:4345–51.
[71] Kang JK, Musgrave CB. The mechanism of HF/H_2O chemical etching of SiO_2. J Chem Phys 2002;116:275–80.